AGU ADVANCING EARTH AND SPACE SCIENCES

Geophysical Research Letters®

RESEARCH LETTER
10.1029/2023GL103745

Characterizing the Role of Non-Linear Interactions in the Transition to Submesoscale Dynamics at a Dense Filament

Mara Freilich[1], **Luc Lenain**[1], **and Sarah T. Gille**[1]

[1]Scripps Institution of Oceanography, University of California San Diego, La Jolla, CA, USA

Key Points:

- Remote sensing observations reveal a kinetic energy spectrum with a continuous slope from 100 to 1 km in an eastern boundary region
- Between 1 and 10 km, ageostrophic non-linear interactions become dynamically important
- Cross-scale kinetic energy transfers computed from 2D velocity observations are associated with shear strain in the observed front

Supporting Information:

Supporting Information may be found in the online version of this article.

Correspondence to:

M. Freilich,
mara_freilich@brown.edu

Citation:

Freilich, M., Lenain, L., & Gille, S. T. (2023). Characterizing the role of non-linear interactions in the transition to submesoscale dynamics at a dense filament. *Geophysical Research Letters*, *50*, e2023GL103745. https://doi.org/10.1029/2023GL103745

Received 20 MAR 2023
Accepted 17 JUL 2023

Author Contributions:

Conceptualization: Mara Freilich, Luc Lenain
Data curation: Mara Freilich, Luc Lenain
Formal analysis: Mara Freilich
Funding acquisition: Mara Freilich
Investigation: Mara Freilich
Methodology: Mara Freilich
Supervision: Sarah T. Gille
Visualization: Mara Freilich
Writing – original draft: Mara Freilich
Writing – review & editing: Luc Lenain, Sarah T. Gille

Abstract Ocean dynamics at the submesoscale play a key role in mediating upper-ocean energy dissipation and dispersion of tracers. Observations of ocean currents from synoptic mesoscale surveys at submesoscale resolution (250 m–100 km) from a novel airborne instrument (MASS DoppVis) reveal that the kinetic energy spectrum in the California Current System is nearly continuous from 100 km to sub-kilometer scales, with a k^{-2} spectral slope. Although there is not a transition in the kinetic energy spectral slope, there is a transition in the dynamics to non-linear ageostrophic interactions at scales of $\mathcal{O}$(1 km). Kinetic energy transfer across spatial scales is enabled by interactions between the rotational and divergent components of the flow field at the submesoscale. Kinetic energy flux is patchy and localized at submesoscale fronts. Kinetic energy is transferred both downscale and upscale from 1 km in the observations of a cold filament.

Plain Language Summary Ocean dynamics at scales of 100 m–10 km, called the submesoscale, are important because they are associated with large velocity gradients and non-linear interactions. Large gradients lead to vertical velocity, which facilitates ocean-atmosphere interactions and ocean biological processes. Velocity gradients and non-linear processes combine to transfer kinetic energy from the large-scale flow to small-scale perturbations. This can lead to instabilities that dissipate energy in the ocean surface layer (rather than the seafloor). Here we analyze novel observations that provide insight into ocean dynamics through the distributions of velocity gradients and energy transfer at 1 km scale. Dynamics at these scales have previously been modeled, but have not been observed directly. We observe a transition where non-linear dynamics become more important at scales of order 10 km. We also introduce new interpretations of spectral analysis (analysis of energy and correlations across scales). Moreover, we analyze covariance of velocity gradient quantities and flow energetics to demonstrate that energy flux is episodic and localized at fronts. Together, these observations demonstrate that fronts play an important role in boundary-layer kinetic energy processes and highlight the evolution of upwelling filaments.

1. Introduction

Ocean processes in the surface boundary layer play a critical role in mediating the influence of atmospheric and climate processes on the ocean. Heating, wind-driven momentum input, and gas exchange occur at the sea surface and are transmitted through the boundary layer and into the ocean interior. The boundary layer also resides in the photic zone, where there is enough light for photosynthesis.

Submesoscale dynamics, the dynamics that operate at the spatial scales between the nearly geostrophically balanced mesoscale eddies (~100 km scales in mid-latitudes) and three-dimensional turbulence (<100 m scales), are particularly important for these boundary layer processes (McWilliams, 2016). Submesoscales influence ocean biogeochemistry by modulating vertical transport (Freilich et al., 2022; Mahadevan, 2016) and influence air-sea interactions by modulating buoyancy and momentum transfer (Strobach et al., 2022). Submesoscale dynamics are hypothesized to facilitate a forward cascade of kinetic energy, resulting in dissipation of eddy kinetic energy in the surface ocean (Barkan et al., 2015; Capet et al., 2008b; Müller et al., 2005; Srinivasan et al., 2023). However, submesoscale dynamics are also known to cascade energy upscale, strengthening mesoscale features (Qiu et al., 2014; Sandery & Sakov, 2017; Schubert et al., 2020). Determining the specifics of the dynamics in this transitional range of 100 m–100 km is essential for quantifying kinetic energy cycles in the ocean (Ferrari & Wunsch, 2009; McWilliams, 2016; Naveira Garabato et al., 2022).

The submesoscale is defined dynamically as the regime where the Rossby number, a non-dimensional parameter defined as $\mathrm{Ro} = U/(fL)$, is order 1 with velocity U, horizontal length scale L, and Coriolis parameter f. While geostrophic dynamics are thought to predominate at the mesoscale and larger, geostrophic balance can begin to

break down at the submesoscale. At the larger end of the submesoscale, the surface quasigeostrophy framework presupposes that surface density fronts modify geostrophic balance (Klein & Lapeyre, 2009), while other theoretical results emphasize the role of non-linear advection in submesoscale dynamics (Barkan et al., 2019).

In this work we characterize the transition to submesoscale dynamics at scales smaller than 10 km and provide observational analysis of the kinetic energy cascade that has been hypothesized from models and theory. We observe submesoscale ocean surface velocity using remote sensing from airplanes during the submesoscale ocean dynamics experiment (S-MODE) field campaign (Farrar et al., 2020). We find substantial kinetic energy at the submesoscale, with a kinetic energy spectral slope that is nearly continuous from 100 to 1 km spatial scales. The dynamics that result in the spatial distribution of kinetic energy at the submesoscale are diagnosed through analysis of velocity cross spectra. These reveal that non-linear interactions between balanced and unbalanced dynamics contribute to submesoscale energy and illuminate the dynamics influencing upper-ocean velocity gradient distributions.

2. Methods

2.1. Remote Sensing

The observations used in this study were collected by the DoppVis instrument (Lenain et al., 2023), a new sensor that is part of the Modular Aerial Sensing System (MASS; Melville et al., 2016), that infers currents from optical observations of the spatio-temporal evolution, that is, dispersion relationship, of surface waves. This method infers the depth-resolved Lagrangian current in the upper ocean. Here, we use the depth averaged current over the upper 2 m. Details about the DoppVis instrument are available in Lenain et al. (2023). The instrument package was installed on a Twin Otter DH-6 aircraft, flying at constant altitude above mean sea level (hereafter, altitude), with a flight profile consisting of repeated reciprocal straight tracks. Consistency between the reciprocal passes is used to validate velocity measurements. Velocity observations are binned to 256 m or 500 m prior to analysis.

Sea surface temperature observations are collected with a Flir SC6700SLS longwave IR camera (1 m resolution) and Heitronics KT19.85 II infrared thermometer (50 m resolution) (see Melville et al., 2016; Lenain et al., 2023, for details).

Observations from two field campaigns are considered in this study. The first field campaign sampled across a cold filament approximately 70 nautical miles offshore of California, as part of the NASA S-MODE program (Farrar et al., 2020). This region is subsequently referred to as the "filament region" and is the focus of this study. These observations occurred on 3 November 2021 from 18:23 to 23:33 UTC while flying at approximately 500 m altitude and on 5 November 2021 from 22:40 to 23:00 UTC while flying at 940 m altitude (Figures 1a–1c).

The higher altitude flight on November 5 enables collection of multiple data points in the cross-swath direction, resulting in a 1.5 km wide swath that is used to compute velocity gradients using central differences. The observations from November 5 are binned at 256 m prior to analysis.

The second field campaign collected observations across two counter-rotating eddies approximately 45 nautical miles offshore of San Diego on 19 May 2021 from 20:56 to 23:26 UTC (Lenain et al., 2023). This region is referred to as the "eddy region." Observations using a vessel mounted acoustic Doppler current profiler (ADCP) were collected under the long northwest-to-southeast leg of the DoppVis observations from 19 May 2021 10:00 to 20 May 2021 13:00 UTC.

Confidence intervals of velocity gradient results including kinetic energy flux and fronotgenesis are estimated using a bootstrapped confidence interval and a velocity error of 0.05 m s^{-1} (Lenain et al., 2023).

The data analyzed to generate each figure is noted in the figure caption and in Table S1 in Supporting Information S1.

2.2. Spectra

We analyze both the kinetic energy spectrum $\left(\hat{E}(f)\right)$ and the cross spectrum $\left(\hat{S}(f)\right)$ with 95% confidence intervals calculated following Bendat and Piersol (2011). Both the kinetic energy spectra and the cross-spectrum between along-track and across-track velocity are computed using Welch's method with Hanning windows.

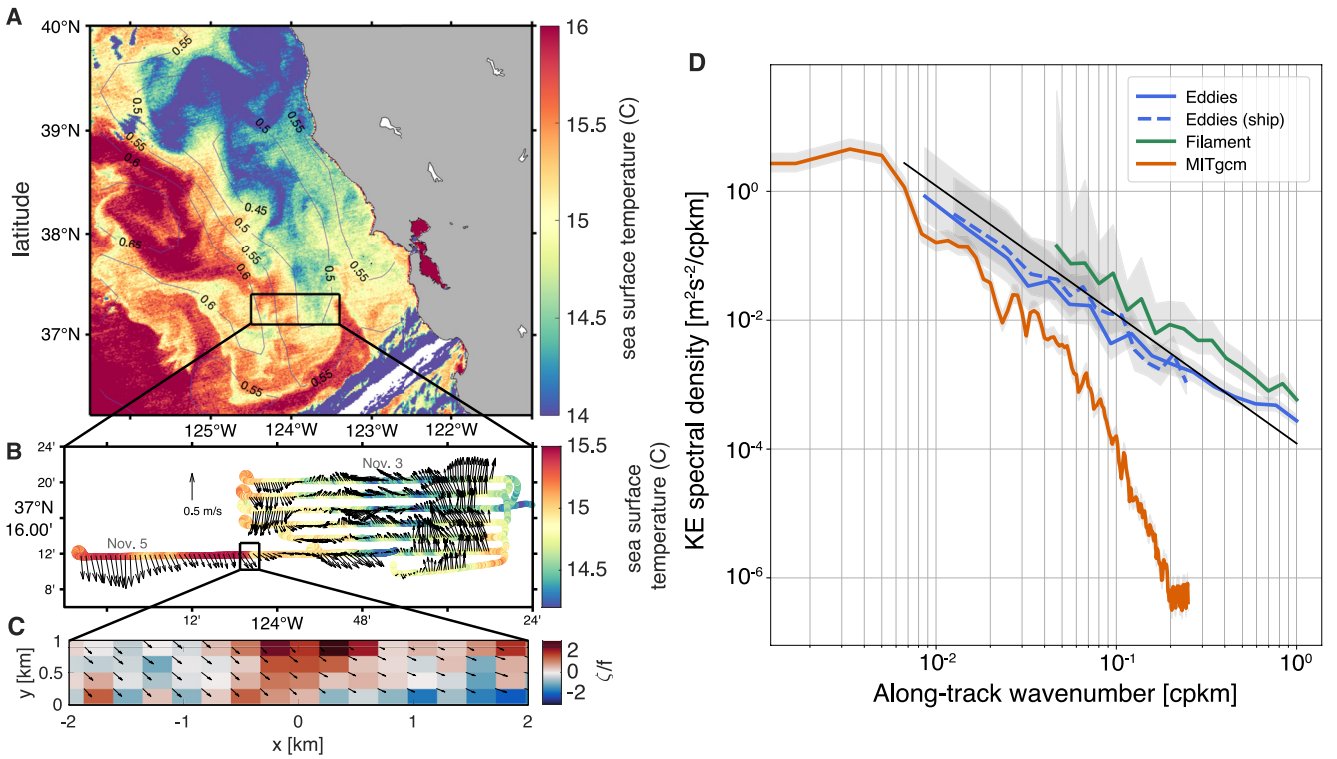

Figure 1. Velocity observations situated in the large-scale context using satellite observations. (a) Satellite (MODIS Aqua) sea surface temperature in the filament region on 4 November 2021 at 21:05Z. Contours show sea surface height from AVISO. (b) DoppVis velocity across the sampled filament (black rectangle in panel (a) is shown as vectors with sea surface temperature from the infrared thermometer. Two days of observations are shown, November 3 and November 5. The filament had shifted on November 5. (c) Vorticity computed from DoppVis in the black rectangle in panel (b) with velocity vectors. This section is shown in Figures 4a and 4b. Velocity gradients in Figures 2 and 4c are computed from the whole transect collected on November 5. (d) Kinetic energy spectral density as a function of along-track wavenumber from a 2 km resolution regional MITgcm model and two observational regions—the eddy region (May 2021) and the filament region (November 2021; panel (b)—and two measurement platforms during May 2021—DoppVis and a ship. The black line shows a k^{-2} spectral slope.

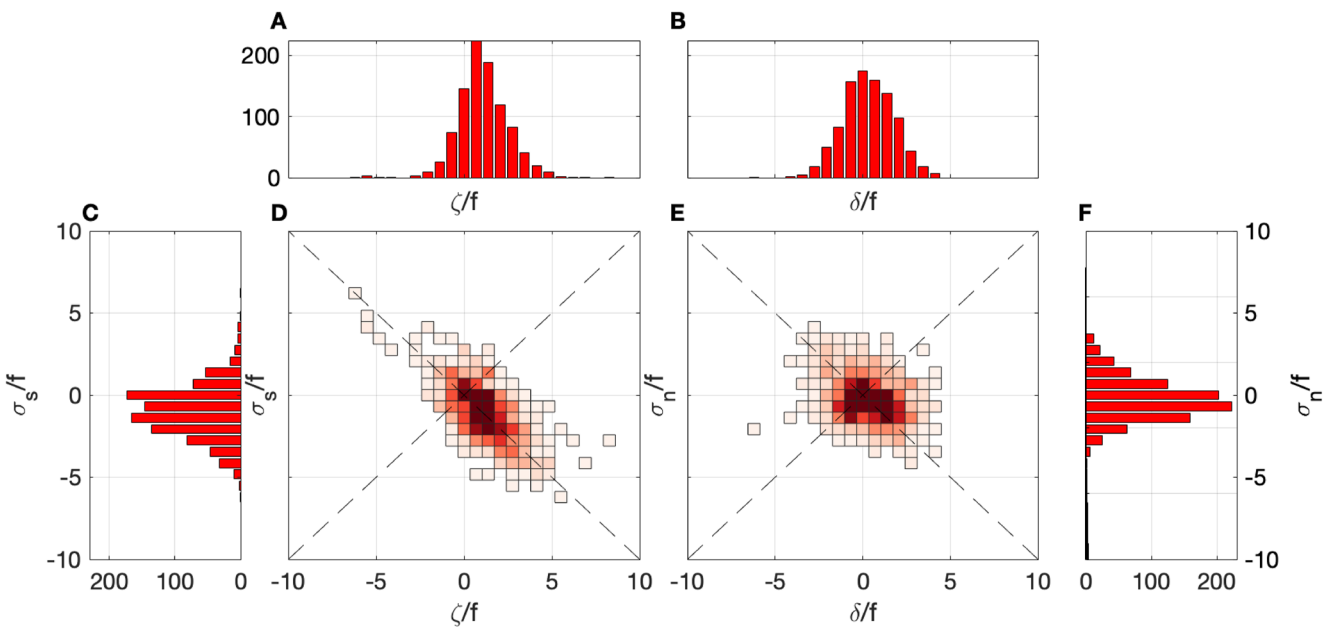

Figure 2. Velocity gradients in the filament observed on October 5 displayed as PDFs of (a) vorticity (ζ), (b) divergence (δ) (c) shear strain (σ_s), and (f) normal strain (σ_n), all normalized by f, along with joint PDFs of normalized vorticity and shear strain (d) and normalized divergence and normal strain (f).

3. Results

3.1. Kinetic Energy Spectrum

The multi-scale nature of the flow is quantified using energy spectra, which can also be used to make inferences about the dominant dynamics governing the flow (Callies & Ferrari, 2013). The filament region is more energetic than the eddy region (Figure 1d), with approximately twice the amount of energy at nearly all spatial scales sampled. The kinetic energy spectra of the DoppVis observations have slopes that are approximately k^{-2} (Figure 1d). The observed kinetic energy spectrum crossing the eddies has magnitude and spectral slope similar to that of the spectra from currents (15 m depth) taken with a vessel mounted ADCP on a nearby transect on the same day for 5–100 km scales.

This analysis extends the observations to smaller spatial scales than have been observed previously. Notably, these scales are smaller than those resolved by state-of-the-art global and regional models. As an example, we show the kinetic energy spectrum from a 2 km grid spacing MITgcm regional model of the California current system (Mazloff et al., 2020) (Figure 1d, red line). This model is forced with ERA5 atmospheric state, Hybrid Coordinate Ocean Model + Navy Coupled Ocean Data Assimilation boundary conditions, and both local and remote tides. The effective resolution of this model is 20 km with the velocity spectrum falling off steeply below that scale due to grid scale dissipation. Even at larger scales, both regions are more energetic than the 2 km grid spacing ocean model of the same region (the eddy region is 5 times more energetic). The discrepancy between model and observations at lower wavenumbers is likely caused by an inverse cascade of submesoscale energy energizing surface mesoscale features in ways that are not represented in the model (Lévy et al., 2001; Mahadevan & Tandon, 2006) and by biased observational sampling toward more energetic features. It is important to note that only the larger end of submesoscale dynamics are resolved by 2 km models (Sinha et al., 2022; Su et al., 2018). This is especially important to keep in mind when considering cross-scale energy fluxes that may be modified by dynamics at small spatial scales.

The observed kinetic energy spectral slopes are consistent with previous observations from this region: a comprehensive analysis of surface velocities measured from vessel-mounted ADCPs in the California Current region from 1993 to 2004 found that the kinetic energy spectral slope in this region is approximately k^{-2} to $k^{-5/3}$ at scales of 10–200 km (Chereskin et al., 2019). This is in contrast to the steeper spectral slope (k^{-3}) in more energetic regions such as the Antarctic Circumpolar Current, which implies geostrophic dynamics (Rocha et al., 2016). Modeling studies in the California Current System have found the kinetic energy spectrum to be continuous from the mesoscale to submesoscale, with a slope of approximately k^{-2} (Capet et al., 2008a).

A range of dynamics could result in the observed spectral slope including internal gravity waves (k^{-2}), surface quasigeostrophy ($k^{-5/3}$), and fronts (k^{-2}) (Boyd, 1992; Lapeyre & Klein, 2006). The observations available in this study cannot sufficiently distinguish these spectral slopes, nor can we identify whether the observed slope has transitions in the submesoscale regime from existing methods. We therefore rely on further analysis to infer the dynamics in this region.

3.2. Distributions of Vorticity, Divergence, and Strain Rate

One of the implications of a kinetic energy spectrum $E(k)$ with a k^{-2} slope is that the velocity derivative spectrum $V(k)$ is flat because the spectra are linked through the relationship $V(k) = k^2E(k)$. Velocity derivatives are essential to understanding and defining the submesoscale, which is defined as Ro$\sim\mathcal{O}(1)$ and where the flow becomes more fully three dimensional (velocity divergence $\delta \sim U/L$). The key velocity derivative quantities, divergence ($\delta = u_x + v_y$), vorticity ($\zeta = v_x - u_y$), and strain are related to each other through a system of coupled non-linear ordinary differential equations (cf. Barkan et al., 2019) and at the submesoscales these non-linear terms become more important. For example, the rate of change of vorticity in an adiabatic system is

$$\frac{D\zeta}{Dt} = -f\delta - \delta\zeta - w_x v_z + w_y u_z. \quad (1)$$

Only the first term on the right hand side, which does not involve a feedback, is present in a quasigeostrophic system. In addition, at the submesoscale the inertial term in the equations of motion ($u \cdot \nabla u \sim U^2/L$) is of the same order as the Coriolis term ($uf \sim Uf$), facilitating cross-scale kinetic energy transfers (Johnson, 2020; Vela-Martín, 2022).

In the observations that allow for computing gradient across the track, which are only available for one track in the filament case (Figures 1b and 1c), we find that the vorticity is skewed positive (skewness 0.54, 90% confidence interval [0.49,0.69]), and the divergence is skewed negative (skewness −0.081, 90% confidence interval [−0.17, 0.043]) (Figures 2a and 2b), consistent with previous (shipboard) observations (Rudnick, 2001; Shcherbina et al., 2015). This skewness can arise from conservation of potential vorticity at fronts. Strain-driven frontogenesis at the sea surface, in the absence of dissipation, results in an infinitely sharp front in finite time with ageostrophic flow that has skewed distributions of divergence (negative) and vorticity (positive) (Barkan et al., 2019; Hoskins & Bretherton, 1972). Compared with anticyclonic fronts, cyclonic fronts are thought to progress more slowly to singularities during frontogenesis, which could result in longer lived cyclonic fronts (Shakespeare, 2016). In addition, the dynamical feedbacks are such that large negative relative vorticity is typically unstable to symmetric and centrifugal instabilities but positive relative vorticity stabilizes the flow to these instabilities, and therefore a skewed distribution develops (Buckingham et al., 2016; Rudnick, 2001). However, it is notable that strain-driven frontogenesis can suppress the growth of symmetric instability (Thomas, 2012), which could reduce the efficiency of this mechanism for generating skewness. Regardless, in boundary layers, negative potential vorticity can arise from frictional and atmospheric forcing, which can trigger symmetric instability.

We next examine the relationship between divergence, vorticity, and strain. The strain is composed of shear strain ($\sigma_s = v_x + u_y$) and normal strain ($\sigma_n = u_x - v_y$). In the filament observations studied here, vorticity is strongly correlated with shear strain (Figure 2d). Vorticity is not passively advected by shear strain and is not directly forced by shear strain (Equation 1), but in an integrated sense vorticity and shear strain become aligned. This correlation can persist due to the relative stability of cyclonic vorticity at straight fronts (Buckingham et al., 2021). This provides an explanation for the strain–vorticity relationship that has been observed in high-resolution simulations (Balwada et al., 2021). However, there is not a strong correlation between divergence and normal strain ($\sigma_n = u_x - v_y$). The lack of correlation is likely due to the short timescales of submesoscale dynamics; while non-zero vorticity can be maintained in an adiabatic system in the absence of divergence and vertical motion, a similar balance does not exist for divergence (Figure 2e).

3.3. Non-Linear Interactions

3.3.1. Interactions Between Rotational and Divergent Flow

The approximately k^{-2} spectral slope in both the filament and eddy regions is informative but inconclusive about the dominant dynamics operating in these regions. The nearly uniform slope across the observed spatial scales leaves open questions about the scales at which a transition to submesoscale dynamics may occur.

The submesoscale feedback between vorticity and divergence (Equation 1) results in a correlation between the geostrophically balanced rotational (streamfunction) flow and the divergent (potential) component of the velocity. These components are not expected to be correlated if waves are not modified by geostrophic or non-wave ageostrophic dynamics (Bôas & Young, 2020). We diagnose when the streamfunction and potential become correlated using the cross spectrum $\left(\hat{S}_{uv}(f)\right)$ between the along-track (u) and cross track (v) velocity components.

When the streamfunction and potential are uncorrelated, as is typically true at the mesoscale and larger, the cross spectrum of the u and v velocity components is a superposition of the spectra of the streamfunction and velocity potential. In this case, since spectra are real, the cross spectrum is real (Bühler et al., 2017). This is a key assumption of the "wave–vortex" decomposition introduced by Bühler et al. (2014). However, when the rotational and divergent flow components correlate, the cross spectrum between the along-track and across-track velocity is complex ($\hat{S}_{uv}(f) = \hat{C}(f) + i\hat{Q}(f)$ where $\hat{Q} \neq 0$). We are therefore able to diagnose the spatial scale where a shift to submesoscale dynamics occurs as the scale at which the cross spectrum becomes complex. We use the cross spectral phase ($\tan(\phi_{uv}(f))$) to summarize this relationship

$$\tan(\phi_{uv}(f)) = \left(\frac{-\hat{Q}(f)}{\hat{C}(f)}\right). \tag{2}$$

The cross spectral phase should only be interpreted in this manner if the coherence, which is the normalized cross spectrum between the along-track and across track velocity, is above the significance threshold (Text S2 in Supporting Information S1).

The squared coherence has contrasting dependence on spatial scale in the two regions studied here (Figure 3a). In the eddy region (blue lines in Figure 3), the squared coherence is large at the largest spatial scales sampled

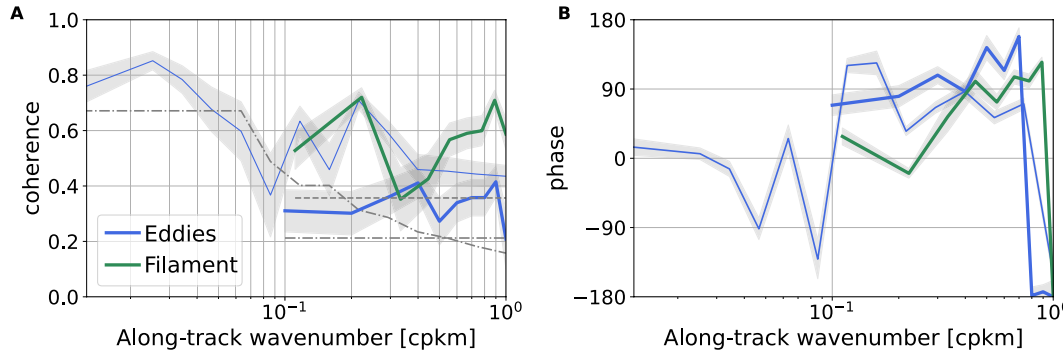

Figure 3. Flow anisotropy and non-linearity revealed by analysis of velocity cross spectrum. (a) Squared coherence as a function of wavenumber. The gray lines show the significance threshold (dashed and dot dash show filament and eddies, respectively) and the shading shows standard deviation. (b) Cross-spectrum phase. The thin lines in show the squared coherence computed from two long transects in the eddy region with 80 km windows while the thick lines show the squared coherence computed from the two long sections and four shorter sections (which crossed the eddy nearly perpendicularly, Figure S1 in Supporting Information S1) using 10 km windows.

(~100 km) and decreases toward smaller spatial scales, but remains significantly different from zero. In the filament region (green lines), the squared coherence is also large at the largest spatial scales sampled (~10 km), decreases at scales larger than 6 km, and then increases again toward the smallest spatial scales sampled (~1 km). Fronts and filaments are expected to be anisotropic at the scale of the feature, as is observed. In all observations considered here, the coherence is large enough to be statistically significant, allowing for analysis of the cross-spectral phase. The only exception is in the eddy region between 0.1 and 0.6 cpkm where the coherence falls below the significance threshold. The phase is noisy in this wavenumber range but is not significant and so should not be interpreted.

The cross-spectral phase summarizes the relationship between the real and imaginary parts of the cross spectrum. When the cross spectrum is purely real, the phase is 0° or 180°; when it is purely imaginary, the phase is ±90°. We find abrupt transitions at a scale slightly smaller than 10 km in the eddy region and 6 km in the filament region, where the imaginary part of the cross spectrum becomes larger than the real part (Figure 3b). This 6 km spatial scale is the same scale where the coherence increases in the filament region (suggesting increased anisotropy), providing consistent evidence of a change to increasingly non-linear frontal dynamics at these scales. By contrast,

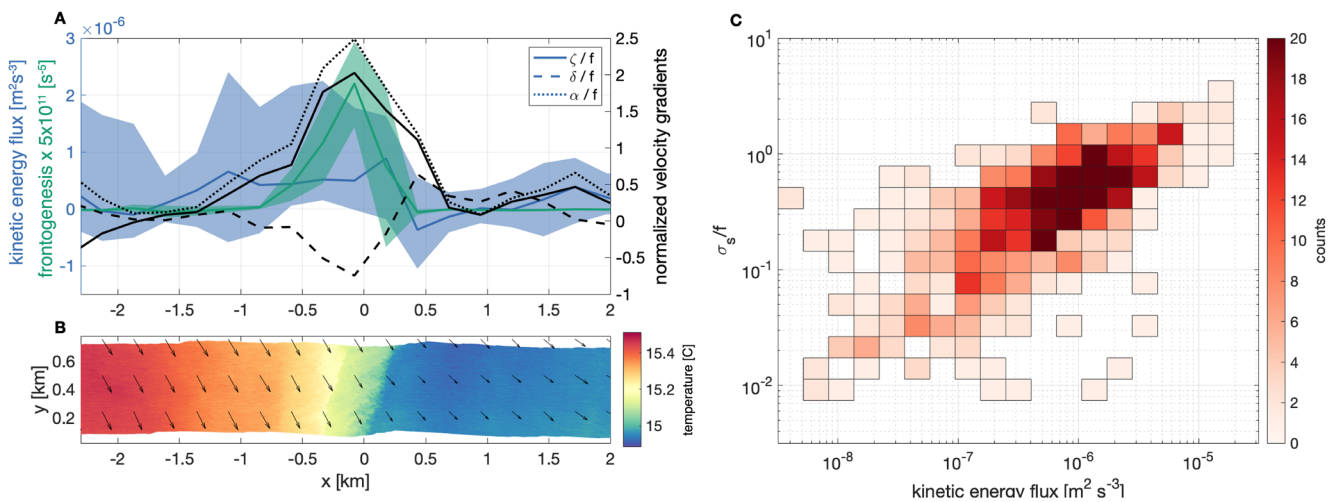

Figure 4. Spatial distribution of kinetic energy flux and frontogenesis from the November 5th filament transect. (a) Kinetic energy flux across 1 km and buoyancy frontogenesis (shading shows the bootstrapped 95% confidence interval) and vorticity, divergence, and strain $\left(\alpha = \sqrt{\sigma_n^2 + \sigma_s^2}\right)$ at one of the fronts on the sampled transect. (b) Sea surface temperature measured from long wave infrared. Velocity is shown with vectors. (c) Joint probability density function of kinetic energy flux from the whole transect and shear strain.

in a surface quasigeostrophic model (Abernathey et al., 2022), which neglects ageostrophic advection, the real part of the cross spectrum dominates at all spatial scales (Figures S2 and S3 in Supporting Information S1). During the eddy observations, the mixed-layer depth was 40–55 m with some regions as shallow as 15 m. In contrast, for the filament observations, the mixed-layer depth was approximately 35 m or shallower and the stratification was approximately 3×10^{-5} s^{-2}. Therefore, the mixed-layer deformation radius was 2–4 km for these locations, implying that the fastest growing baroclinic mode is around 8–24 km (Dong et al., 2020). Thus, the transition to non-linear ageostrophic dynamics observed here occurs in the approximate range of the scale of mixed-layer baroclinic instability.

There are a number of mechanisms that could be responsible for the interaction between rotational and divergent velocity. In the filament case, the interaction of the ageostrophic frontal divergence and larger scale geostrophic flow is likely the dominant mechanism. Here we find that the shift to a mostly imaginary cross spectrum is localized in the regions of largest velocity gradient (Figure S4 in Supporting Information S1). The eddy case likely encompasses a larger range of dynamics, including near-inertial oscillations modified by the vorticity of the observed features, frontal dynamics, and submesoscale vortices.

3.3.2. Spectral Energy Transfers

The distribution of kinetic energy across spatial scales reflects dynamics that are local in wavenumber, but importantly also reflects energy transfers across scales. At the submesoscale, major open questions remain regarding the direction of the energy cascade, the mechanisms that lead to a forward energy, and the rate of the forward energy cascade (McWilliams, 2016; Müller et al., 2005). Forward energy flux precedes dissipation at small spatial scales by turbulent processes.

The energy transfer across scales can be quantified using coarse graining (Aluie et al., 2018; Eyink, 2005; Germano, 1992). The kinetic energy flux is defined here as

$$\Pi = -\left(\tau_{uv}\left(\bar{u}_y + \bar{v}_x\right) + \tau_{uu}\bar{u}_x + \tau_{vv}\bar{v}_y\right) \tag{3}$$

where $\tau_{ab} = \overline{ab} - \bar{a}\ \bar{b}$ and $\bar{\cdot}$ is a top hat filter. Positive (negative) values indicate a flux of energy toward smaller (larger) spatial scales. We use velocity observed on a 256 m grid and a top hat filter with a scale of 1 km to compute an instantaneous energy flux across the observed transect.

In the frontal regions in this flow, there is a strong forward energy flux localized in a 1 km region at the frontal outcrop, where there is also a peak in frontogenesis (Figures 4a and 4b). The energy flux to smaller spatial scales is driven by the first term in Equation 3 (Figure S5 in Supporting Information S1). This term involves the shear strain multiplied by the scale-dependent covariance between the along-track and cross-track velocity. In fact, over the entire 60 km section, there is a strong correlation between the shear strain and the kinetic energy flux (Figure 4c).

The influence of the shear strain on the kinetic energy flux is modulated by the covariance between the u and v velocity components (or, equivalently, the anistropy of the flow), which becomes large below scales of 6 km in this filament region (Figure 3a). Barotropic shear instabilities extract kinetic energy from sheared mean flows when smaller scale features lean into the shear, resulting in a forward energy cascade.

The observed kinetic energy flux is patchy (Figure 4c), with the largest flux concentrated in small spatial scales even within the 60 km filament region observed here. On this whole transect, the kinetic energy flux varies over three orders of magnitude (Figure 4c). The typical kinetic energy flux across 1 km in the filament region is $\mathcal{O}\left(10^{-6}\ \mathrm{m^2\ s^{-3}}\right)$. This rate is about an order of magnitude larger than the kinetic energy flux obtained from mooring based observations using a filter scale of 5 days (Naveira Garabato et al., 2022), drifter based observations at 1 km scale that average over a large region of the northern Gulf of Mexico (Balwada et al., 2022), and a model at 500 m spatial resolution (Srinivasan et al., 2023). Given that we present direct observations of the kinetic energy flux terms, this suggests that the magnitude of instantaneous kinetic energy flux has been underestimated by previous modeling and observational work.

4. Discussion and Conclusion

The airborne observations presented here reveal large and patchy kinetic energy flux localized at submesoscale fronts and advance observational characterization of submesoscale dynamics. The synoptic sampling from submesoscale to mesoscale allows us to extend an observational kinetic energy spectrum to scales below 1 km.

Dense filaments such as the one observed here have an important role in the energetics of upwelling systems with submesoscale dynamics influencing the fate of upwelled waters.

We demonstrate that although there is not a clear change in the kinetic energy spectral slope, there is a transition in the dynamics to non-linear interactions that characterize submesoscales at scales of 6–10 km. In particular, this transition is characterized by the interaction between divergent and rotational velocity components. This transition would not occur with surface quasigeostrophic dynamics, and we attribute it instead to a dominance of ageostrophic dynamics in the observations.

The observed transition to non-linearity has important implications for observations of ocean velocity from remote sensing. For example, the SWOT mission aims to infer mesoscale to submesoscale velocities through observation of sea surface height. These velocities are computed through geostrophic balance, which only accounts for the rotational component of the flow (but does not include higher order rotational velocity components). Not only do we find that a significant amount of the kinetic energy is likely in the divergent component of the flow at scales below 10 km in this region—and potentially at larger scales in more energetic regions (Callies et al., 2015)—but also that the rotational and divergent flows interact such that filtering of the divergent processes (e.g., waves) to recover the rotational component of the flow may be more challenging.

These observations are also the first direct observations of *snapshots* of kinetic energy flux and frontogenesis in the ocean. This allows us to investigate the relationships between the kinetic energy flux and hydrographic features. We find that kinetic energy flux is patchy but can be large (10^{-6} m^2 s^{-3}) at submesoscale fronts. The patchiness of kinetic energy flux has important implications for resolving the dynamics that contribute to an energy cascade. Due to the difficulty resolving scales ranging from mesoscale straining to turbulent dissipation in models, these observations—where that challenge is observationally addressed using a novel remote sensing platform—are particularly valuable. These aircraft measurements provide a preview of what might be possible from future satellite-based radar snapshots from platforms such as Harmony and SEASTAR (Gommenginger et al., 2019; López-Dekker et al., 2019). In these observations, kinetic energy is transferred both downscale and upscale from 1 km.

Recent modeling work has suggested that resolving frontogenesis is essential to accurate representation of submesoscale kinetic energy transfers (Naveira Garabato et al., 2022; Srinivasan et al., 2023). The observations analyzed here demonstrate a large forward energy transfer localized at fronts, although not exclusively during active large-scale frontogenesis. Recent work in the Gulf of Mexico, another region with an active submesoscale, has hinted that a forward cascade of kinetic energy occurs at scales of 500 m–5 km (Balwada et al., 2022) in observations (with smaller scales during the summer) and at scales of 5 km in models (Srinivasan et al., 2023).

The modeling study of Sullivan and McWilliams (2018), which simulated a dense filament, also found an important role for the horizontal Reynolds stress term ($u'v'v_x$) during the frontal arrest phase of a dense filament, which is consistent with our observation that the shear strain term dominated kinetic energy flux. This relationship may arise from certain aspects of the feature studied here and may not generalize to all fronts. For example, Srinivasan et al. (2023) analyzed kinetic energy fluxes in 500 m and 2 km resolution ocean models, which resolve dynamics at larger scales than those that are the focus of our study. They find an equipartition between strain-driven and convergence-driven forward energy cascade at submesoscale scales (Srinivasan et al., 2023). While we observe that the forward energy transfer is strain-driven in our observations, it is important to note that we have only one snapshot of a filament that appears to be partially restratifying, so this does not invalidate the role of convergence in forward energy flux.

These results suggest an out-sized role for fronts and filaments as hotspots of surface kinetic energy flux. Barotropic energy transfer is enabled by interactions between the rotational and divergent components of the flow field at submesoscale fronts. Fronts are spatially inhomogeneously distributed in the ocean and vary seasonally (Drushka et al., 2019; Mauzole et al., 2020), but the distributions of fronts are distinct from the distributions of mesoscale kinetic energy (Busecke & Abernathey, 2019). Surface kinetic energy dissipation may similarly vary substantially in space and time, but understanding how it varies relies on increased mechanistic understanding of the energetics of submesoscale features. Disentangling these would require more observations to establish the effect of particular submesoscale features on the regional statistics.

Data Availability Statement

All presented data are available at UCSD Library Digital Collection, https://doi.org/10.6075/J0F76CRK.

Acknowledgments
We would like to thank Nick Statom for data collection and Alex Andriatis for ship observations. We would like to acknowledge Matthew Mazloff, Peter Franks, Oliver Buhler, Roy Barkan, Jacob Wenegrat, and the S-MODE science team, and particularly J. Thomas Farrar, for discussions about this work and Dhruv Balwada, Han Wang, and an anonymous reviewer for constructive comments on the manuscript. This work was funded by a Scripps Institutional Postdoctoral fellowship and by the Physical Oceanography programs at ONR (Grant N00014-19-1-2635), and NASA (Grants 80NSSC19K1688, 80NSSC20K1136, and 80NSSC21K1822).

References

Abernathey, R., Rocha, C. B., Ross, A., Jansen, M., Li, Z., Poulin, F. J., et al. (2022). pyqg/pyqg: v0.7.2. *Zenodo*. https://doi.org/10.5281/zenodo.6563667

Aluie, H., Hecht, M., & Vallis, G. K. (2018). Mapping the energy cascade in the North Atlantic Ocean: The coarse-graining approach. *Journal of Physical Oceanography*, *48*(2), 225–244. https://doi.org/10.1175/JPO-D-17-0100.1

Balwada, D., Xiao, Q., Smith, S., Abernathey, R., & Gray, A. R. (2021). Vertical fluxes conditioned on vorticity and strain reveal submesoscale ventilation. *Journal of Physical Oceanography*, *51*(9), 2883–2901. https://doi.org/10.1175/JPO-D-21-0016.1

Balwada, D., Xie, J.-H., Marino, R., & Feraco, F. (2022). Direct observational evidence of an oceanic dual kinetic energy cascade and its seasonality. *Science Advances*, *8*(41), eabq2566. https://doi.org/10.1126/sciadv.abq2566

Barkan, R., Molemaker, M. J., Srinivasan, K., McWilliams, J. C., & D'Asaro, E. A. (2019). The role of horizontal divergence in submesoscale frontogenesis. *Journal of Physical Oceanography*, *49*(6), 1593–1618. https://doi.org/10.1175/jpo-d-18-0162.1

Barkan, R., Winters, K. B., & Smith, S. G. L. (2015). Energy cascades and loss of balance in a reentrant channel forced by wind stress and buoyancy fluxes. *Journal of Physical Oceanography*, *45*(1), 272–293. https://doi.org/10.1175/JPO-D-14-0068.1

Bendat, J. S., & Piersol, A. G. (2011). *Random data: Analysis and measurement procedures*. John Wiley & Sons.

Bôas, A. B. V., & Young, W. R. (2020). Directional diffusion of surface gravity wave action by ocean macroturbulence. *Journal of Fluid Mechanics*, *890*, R3. https://doi.org/10.1017/jfm.2020.116

Boyd, J. P. (1992). The energy spectrum of fronts: Time evolution of shocks in burgers equation. *Journal of the Atmospheric Sciences*, *49*(2), 128–139. https://doi.org/10.1175/1520-0469(1992)049⟨0128:TESOFT⟩2.0.CO;2

Buckingham, C. E., Gula, J., & Carton, X. (2021). The role of curvature in modifying frontal instabilities. Part I: Review of theory and presentation of a nondimensional instability criterion. *Journal of Physical Oceanography*, *51*(2), 299–315. https://doi.org/10.1175/jpo-d-19-0265.1

Buckingham, C. E., Naveira Garabato, A. C., Thompson, A. F., Brannigan, L., Lazar, A., Marshall, D. P., et al. (2016). Seasonality of submesoscale flows in the ocean surface boundary layer. *Geophysical Research Letters*, *43*(5), 2118–2126. https://doi.org/10.1002/2016GL068009

Bühler, O., Callies, J., & Ferrari, R. (2014). Wave–vortex decomposition of one-dimensional ship-track data. *Journal of Fluid Mechanics*, *756*, 1007–1026. https://doi.org/10.1017/jfm.2014.488

Bühler, O., Kuang, M., & Tabak, E. G. (2017). Anisotropic Helmholtz and wave–vortex decomposition of one-dimensional spectra. *Journal of Fluid Mechanics*, *815*, 361–387. https://doi.org/10.1017/jfm.2017.57

Busecke, J. J. M., & Abernathey, R. P. (2019). Ocean mesoscale mixing linked to climate variability. *Science Advances*, *5*(1), eaav5014. https://doi.org/10.1126/sciadv.aav5014

Callies, J., & Ferrari, R. (2013). Interpreting energy and tracer spectra of upper-ocean turbulence in the submesoscale range (1–200 km). *Journal of Physical Oceanography*, *43*(11), 2456–2474. https://doi.org/10.1175/jpo-d-13-063.1

Callies, J., Ferrari, R., Klymak, J. M., & Gula, J. (2015). Seasonality in submesoscale turbulence. *Nature Communications*, *6*(1), 1–8. https://doi.org/10.1038/ncomms7862

Capet, X., McWilliams, J. C., Molemaker, M. J., & Shchepetkin, A. (2008a). Mesoscale to submesoscale transition in the California Current System. Part I: Flow structure, eddy flux, and observational tests. *Journal of Physical Oceanography*, *38*(1), 29–43. https://doi.org/10.1175/2007jpo3671.1

Capet, X., McWilliams, J. C., Molemaker, M. J., & Shchepetkin, A. F. (2008b). Mesoscale to submesoscale transition in the California current system. Part III: Energy balance and flux. *Journal of Physical Oceanography*, *38*(10), 2256–2269. https://doi.org/10.1175/2008JPO3810.1

Chereskin, T. K., Rocha, C. B., Gille, S. T., Menemenlis, D., & Passaro, M. (2019). Characterizing the transition from balanced to unbalanced motions in the southern California current. *Journal of Geophysical Research: Oceans*, *124*(3), 2088–2109. https://doi.org/10.1029/2018JC014583

Dong, J., Fox-Kemper, B., Zhang, H., & Dong, C. (2020). The scale of submesoscale baroclinic instability globally. *Journal of Physical Oceanography*, *50*(9), 2649–2667. https://doi.org/10.1175/JPO-D-20-0043.1

Drushka, K., Asher, W. E., Sprintall, J., Gille, S. T., & Hoang, C. (2019). Global patterns of submesoscale surface salinity variability. *Journal of Physical Oceanography*, *49*(7), 1669–1685. https://doi.org/10.1175/JPO-D-19-0018.1

Eyink, G. L. (2005). Locality of turbulent cascades. *Physica D: Nonlinear Phenomena*, *207*(1), 91–116. https://doi.org/10.1016/j.physd.2005.05.018

Farrar, J. T., D'Asaro, E., Rodriguez, E., Shcherbina, A., Czech, E., Matthias, P., et al. (2020). S-MODE: The sub-mesoscale ocean dynamics experiment. In *IGARSS 2020—2020 IEEE international geoscience and remote sensing symposium* (pp. 3533–3536). https://doi.org/10.1109/IGARSS39084.2020.9323112

Ferrari, R., & Wunsch, C. (2009). Ocean circulation kinetic energy: Reservoirs, sources, and sinks. *Annual Review of Fluid Mechanics*, *41*(1), 253–282. https://doi.org/10.1146/annurev.fluid.40.111406.102139

Freilich, M., Flierl, G., & Mahadevan, A. (2022). Diversity of growth rates maximizes phytoplankton productivity in an eddying ocean. *Geophysical Research Letters*, *49*(3), e2021GL096180. https://doi.org/10.1029/2021GL096180

Germano, M. (1992). Turbulence: The filtering approach. *Journal of Fluid Mechanics*, *238*, 325–336. https://doi.org/10.1017/S0022112092001733

Gommenginger, C., Chapron, B., Hogg, A., Buckingham, C., Fox-Kemper, B., Eriksson, L., et al. (2019). SEASTAR: A mission to study ocean submesoscale dynamics and small-scale atmosphere-ocean processes in coastal, shelf and polar seas. *Frontiers in Marine Science*, *6*. https://doi.org/10.3389/fmars.2019.00457

Hoskins, B. J., & Bretherton, F. P. (1972). Atmospheric frontogenesis models: Mathematical formulation and solution. *Journal of the Atmospheric Sciences*, *29*(1), 11–37. https://doi.org/10.1175/1520-0469(1972)029<0011:afmmfa>2.0.co;2

Johnson, P. L. (2020). Energy transfer from large to small scales in turbulence by multiscale nonlinear strain and vorticity interactions. *Physical Review Letters*, *124*(10), 104501. https://doi.org/10.1103/physrevlett.124.104501

Klein, P., & Lapeyre, G. (2009). The oceanic vertical pump induced by mesoscale and submesoscale turbulence. *Annual Review of Marine Science*, *1*(1), 351–375. https://doi.org/10.1146/annurev.marine.010908.163704

Lapeyre, G., & Klein, P. (2006). Impact of the small-scale elongated filaments on the oceanic vertical pump. *Journal of Marine Research*, *64*(6), 835–851. (Publisher: Sears Foundation for Marine Research). https://doi.org/10.1357/002224006779698369

Lenain, L., Smeltzer, B. K., Pizzo, N., Freilich, M., Colosi, L., Ellingsen, S. Å., et al. (2023). Airborne remote sensing of upper-ocean and surface properties, currents and their gradients from meso to submesoscales. *Geophysical Research Letters*, *50*(8), e2022GL102468. https://doi.org/10.1029/2022GL102468

Lévy, M., Klein, P., & Treguier, A.-M. (2001). Impact of sub-mesoscale physics on production and subduction of phytoplankton in an oligotrophic regime. *Journal of Marine Research*, *59*(4), 535–565. (Publisher: Sears Foundation for Marine Research). https://doi.org/10.1357/002224001762842181

López-Dekker, P., Rott, H., Prats-Iraola, P., Chapron, B., Scipal, K., & Witte, E. D. (2019). Harmony: An Earth explorer 10 mission candidate to observe land, ice, and ocean surface dynamics. In *IGARSS 2019—2019 IEEE international geoscience and remote sensing symposium* (pp. 8381–8384). https://doi.org/10.1109/IGARSS.2019.8897983

Mahadevan, A. (2016). The impact of submesoscale physics on primary productivity of plankton. *Annual Review of Marine Science*, *8*(1), 161–184. (Publisher: Annual Reviews). https://doi.org/10.1146/annurev-marine-010814-015912

Mahadevan, A., & Tandon, A. (2006). An analysis of mechanisms for submesoscale vertical motion at ocean fronts. *Ocean Modelling*, *14*(3–4), 241–256. https://doi.org/10.1016/j.ocemod.2006.05.006

Mauzole, Y. L., Torres, H. S., & Fu, L.-L. (2020). Patterns and dynamics of SST fronts in the California current system. *Journal of Geophysical Research: Oceans*, *125*(2), e2019JC015499. https://doi.org/10.1029/2019JC015499

Mazloff, M. R., Cornuelle, B., Gille, S. T., & Wang, J. (2020). The importance of remote forcing for regional modeling of internal waves. *Journal of Geophysical Research: Oceans*, *125*(2), e2019JC015623. https://doi.org/10.1029/2019JC015623

McWilliams, J. C. (2016). Submesoscale currents in the ocean. *Proceedings of the Royal Society A: Mathematical, Physical and Engineering Sciences*, *472*(2189), 20160117. https://doi.org/10.1098/rspa.2016.0117

Melville, W. K., Lenain, L., Cayan, D. R., Kahru, M., Kleissl, J. P., Linden, P. F., & Statom, N. M. (2016). The modular aerial sensing system. *Journal of Atmospheric and Oceanic Technology*, *33*(6), 1169–1184. https://doi.org/10.1175/JTECH-D-15-0067.1

Müller, P., McWilliams, J. C., & Molemaker, M. J. (2005). Routes to dissipation in the ocean: The 2D/3D turbulence conundrum. In *Marine turbulence: Theories, observations and models* (pp. 397–405). Cambridge University Press.

Naveira Garabato, A. C., Yu, X., Callies, J., Barkan, R., Polzin, K. L., Frajka-Williams, E. E., et al. (2022). Kinetic energy transfers between mesoscale and submesoscale motions in the open ocean's upper layers. *Journal of Physical Oceanography*, *52*(1), 75–97. https://doi.org/10.1175/JPO-D-21-0099.1

Qiu, B., Chen, S., Klein, P., Sasaki, H., & Sasai, Y. (2014). Seasonal mesoscale and submesoscale eddy variability along the North Pacific subtropical countercurrent. *Journal of Physical Oceanography*, *44*(12), 3079–3098. https://doi.org/10.1175/jpo-d-14-0071.1

Rocha, C. B., Chereskin, T. K., Gille, S. T., & Menemenlis, D. (2016). Mesoscale to submesoscale wavenumber spectra in Drake Passage. *Journal of Physical Oceanography*, *46*(2), 601–620. https://doi.org/10.1175/jpo-d-15-0087.1

Rudnick, D. L. (2001). On the skewness of vorticity in the upper ocean. *Geophysical Research Letters*, *28*(10), 2045–2048. https://doi.org/10.1029/2000GL012265

Sandery, P. A., & Sakov, P. (2017). Ocean forecasting of mesoscale features can deteriorate by increasing model resolution towards the submesoscale. *Nature Communications*, *8*(1), 1566. https://doi.org/10.1038/s41467-017-01595-0

Schubert, R., Gula, J., Greatbatch, R. J., Baschek, B., & Biastoch, A. (2020). The submesoscale kinetic energy cascade: Mesoscale absorption of submesoscale mixed layer eddies and frontal downscale fluxes. *Journal of Physical Oceanography*, *50*(9), 2573–2589. https://doi.org/10.1175/JPO-D-19-0311.1

Shakespeare, C. J. (2016). Curved density fronts: Cyclogeostrophic adjustment and frontogenesis. *Journal of Physical Oceanography*, *46*(10), 3193–3207. https://doi.org/10.1175/JPO-D-16-0137.1

Shcherbina, A. Y., Sundermeyer, M. A., Kunze, E., D'Asaro, E., Badin, G., Birch, D., et al. (2015). The LatMix summer campaign: Submesoscale stirring in the upper ocean. *Bulletin of the American Meteorological Society*, *96*(8), 1257–1279. https://doi.org/10.1175/bams-d-14-00015.1

Sinha, A., Callies, J., & Menemenlis, D. (2022). Do submesoscales affect the large-scale structure of the upper ocean? *Journal of Physical Oceanography*, *1*(4), 1025–1040. https://doi.org/10.1175/JPO-D-22-0129.1

Srinivasan, K., Barkan, R., & McWilliams, J. C. (2023). A forward energy flux at submesoscales driven by frontogenesis. *Journal of Physical Oceanography*, *53*(1), 287–305. https://doi.org/10.1175/JPO-D-22-0001.1

Strobach, E., Klein, P., Molod, A., Fahad, A. A., Trayanov, A., Menemenlis, D., & Torres, H. (2022). Local air-sea interactions at ocean mesoscale and submesoscale in a western boundary current. *Geophysical Research Letters*, *49*(7), e2021GL097003. https://doi.org/10.1029/2021GL097003

Su, Z., Wang, J., Klein, P., Thompson, A. F., & Menemenlis, D. (2018). Ocean submesoscales as a key component of the global heat budget. *Nature Communications*, *9*(1), 775. https://doi.org/10.1038/s41467-018-02983-w

Sullivan, P. P., & McWilliams, J. C. (2018). Frontogenesis and frontal arrest of a dense filament in the oceanic surface boundary layer. *Journal of Fluid Mechanics*, *837*, 341–380. https://doi.org/10.1017/jfm.2017.833

Thomas, L. N. (2012). On the effects of frontogenetic strain on symmetric instability and inertia–gravity waves. *Journal of Fluid Mechanics*, *711*, 620–640. https://doi.org/10.1017/jfm.2012.416

Vela-Martín, A. (2022). The energy cascade as the origin of intense events in small-scale turbulence. *Journal of Fluid Mechanics*, *937*, A13. https://doi.org/10.1017/jfm.2022.117